

---

# FROM SPARSE SENSORS TO CONTINUOUS FIELDS: STRIDE FOR SPATIOTEMPORAL RECONSTRUCTION

---

**Yanjie Tong, Peng Chen**

School of Computational Science and Engineering

Georgia Institute of Technology

Atlanta, GA 30332

{ytong80, pchen402}@gatech.edu

## ABSTRACT

Reconstructing high-dimensional spatiotemporal fields from sparse point-sensor measurements is a central challenge in learning parametric PDE dynamics. Existing approaches often struggle to generalize across trajectories and parameter settings, or rely on discretization-tied decoders that do not naturally transfer across meshes and resolutions. We propose STRIDE (Spatio-Temporal Recurrent Implicit DEcoder), a two-stage framework that maps a short window of sensor measurements to a latent state with a temporal encoder and reconstructs the field at arbitrary query locations with a modulated implicit neural representation (INR) decoder. Using the Fourier Multi-Component and Multi-Layer Neural Network (FMMNN) as the INR backbone improves representation of complex spatial fields and yields more stable optimization than sine-based INRs. We provide a conditional theoretical justification: under stable delay observability of point measurements on a low-dimensional parametric invariant set, the reconstruction operator factors through a finite-dimensional embedding, making STRIDE-type architectures natural approximators. Experiments on four challenging benchmarks spanning chaotic dynamics and wave propagation show that STRIDE outperforms strong baselines under extremely sparse sensing, supports super-resolution, and remains robust to noise.

## 1 Introduction

Many scientific and engineering systems are governed by nonlinear partial differential equations (PDEs) and evolve on high-dimensional spatiotemporal fields that depend on parameters (e.g., forcing, geometry, material properties, or initial/boundary conditions) [1, 2]. In practice, however, measurements are often restricted to sparse point sensors, so recovering the full field amounts to an ill-posed state estimation problem [3]. Although high-fidelity solvers can produce accurate trajectories, their computational cost limits repeated simulation across parameter settings and real-time deployment [4]. These constraints motivate learned surrogates that reconstruct full spatiotemporal states from sparse measurements while generalizing across trajectories and (possibly unobserved) parameters.

Existing data-driven approaches for mapping sparse observations to full states fall broadly into two categories: methods that reconstruct from concurrent measurements only [5, 6], and methods that explicitly exploit temporal history (e.g., delay embeddings or recurrent state estimators) [7, 8, 9, 10]. The former can perform well when the mapping is nearly instantaneous, but can struggle in parametric or chaotic regimes where the same sensor snapshot may correspond to multiple underlying states. The latter reduce this ambiguity by using a short observation window, echoing classical embedding and observability ideas [11, 12], but many existing designs still rely on decoders tied to a fixed discretization or whose parameter count scales with the output dimension, limiting transfer to irregular meshes and varying resolutions.

A complementary approach is to represent fields with *implicit neural representations* (INRs), i.e., continuous coordinate-to-field maps that can be queried at arbitrary locations, naturally supporting irregular meshes and super-resolution. Among INR backbones, SIREN has demonstrated strong expressivity via sine activations [13]. In PDE learning, modulated INRs (e.g., FiLM-modulated SIREN) have been used in operator learning and spatiotemporal prediction [14, 15, 16]. While sine-activated networks like SIREN are expressive, they often encounter challenging optimization

landscapes when modeling high-frequency content. To address this, the Fourier Multi-Component and Multi-Layer Neural Network (FMMNN) was recently introduced to enhance optimization stability and improve the representation of fine-scale spatial structures [17].

We propose STRIDE (Spatio-Temporal Recurrent Implicit DEcoder), a two-stage framework that combines windowed sensor history with continuous decoding. STRIDE maps a short observation window to a low-dimensional latent state with a temporal encoder (e.g., LSTM [18], or alternatives such as Mamba [19]) and reconstructs the field at arbitrary query locations with a modulated INR decoder. Our default instantiation uses FMMNN with lightweight shift modulations, enabling resolution-invariant reconstruction while improving training stability relative to sine-based backbones. We further provide a conditional theoretical justification: under stable delay observability of point measurements on an effectively low-dimensional parametric invariant set (Mañé-type projection results [20]), the reconstruction operator factors through a finite-dimensional embedding, making STRIDE-type architectures natural approximators.

### Our contributions:

- **Two-stage sparse sensors to continuous field reconstruction.** We introduce STRIDE, which combines a window encoder (history/delay information) with a modulated INR decoder to reconstruct continuous spatiotemporal fields from sparse point sensors in multi-trajectory, parametric PDE settings, without assuming the parameters are observed at inference.
- **Discretization- and resolution-invariant decoding.** By decoding through a coordinate-based INR and training with randomized spatial sampling, STRIDE applies to irregular meshes and supports super-resolution by querying the decoder at arbitrary locations.
- **Stable, powerful INR decoding via FMMNN.** We develop an INR decoder design based on FMMNN with shift modulations, yielding improved representation of spatial fields and favorable training dynamics compared to modulated SIREN backbones.
- **Conditional theoretical justification.** Under a stable delay-observability assumption on an effectively low-dimensional parametric invariant set, we formalize the existence and stability of the reconstruction operator and show that it factors through a finite-dimensional embedding, supporting STRIDE-type approximations.
- **Extensive empirical evaluation.** We benchmark STRIDE on four challenging datasets (chaotic dynamics, fluid flow, shallow water, and seismic wave propagation) and provide ablations over sensor budgets, window length, noise, spatial resolutions, and architectural choices (temporal encoders and INR backbones).

Paper organization: Section 2 presents STRIDE, Section 3 provides the theoretical justification based on delay observability, Section 4 reports the main experiments, and Section 5 concludes with limitations and future directions.

## 2 Method: STRIDE

In this section, we present STRIDE, a two-stage framework that (i) encodes a short history of sparse point-sensor measurements into a latent state with a temporal encoder and (ii) decodes this latent state into a continuous spatial field via a modulated implicit neural representation (INR). We describe the observation model, the two-stage mapping, architectural instantiations, and the training procedure.

### 2.1 Setting and Observation Model

Consider a *parametric* spatiotemporal dynamical system (e.g., a PDE) on a spatial domain  $\Omega \subset \mathbb{R}^{d_\xi}$  indexed by a parameter  $\mu \in \mathcal{P} \subset \mathbb{R}^{d_\mu}$ . For a fixed  $\mu$ , the state at discrete time index  $t$  is a vector-valued field  $\mathbf{x}_t(\cdot; \mu) : \Omega \rightarrow \mathbb{R}^{d_x}$ ; we write its pointwise value as  $\mathbf{x}(\xi, t; \mu) := \mathbf{x}_t(\xi; \mu)$  for  $\xi \in \Omega$ .

We observe the system through  $N_s$  point sensors at locations  $\{\xi^{(1)}, \dots, \xi^{(N_s)}\} \subset \Omega$  and a fixed channel projection  $\Pi : \mathbb{R}^{d_x} \rightarrow \mathbb{R}^{d_o}$  selecting the observed  $d_o$  channels. The measurement vector at time  $t$  is

$$\mathbf{y}_t(\mu) := (\Pi \mathbf{x}(\xi^{(1)}, t; \mu), \dots, \Pi \mathbf{x}(\xi^{(N_s)}, t; \mu)) \in \mathbb{R}^p, \quad p = N_s d_o. \quad (1)$$

Given an observation window  $\mathbf{y}_{t-k:t}(\mu) = \{\mathbf{y}_{t-k}(\mu), \dots, \mathbf{y}_t(\mu)\}$  and a query point  $\xi$ , our goal is to reconstruct the full field at time  $t$ , i.e., to predict  $\mathbf{x}(\xi, t; \mu)$  for arbitrary  $\xi$ , uniformly over  $\mu \in \mathcal{P}$ . We often omit the dependence on  $\mu$  for readability. At inference time,  $\mu$  is not assumed to be observed, and STRIDE takes only the measurement window  $\mathbf{y}_{t-k:t} = \{\mathbf{y}_{t-k}, \dots, \mathbf{y}_t\}$  as input.

## 2.2 Two-Stage Architecture

STRIDE consists of a temporal (window) encoder  $\mathcal{G}$  that maps the observation window  $\mathbf{y}_{t-k:t}$  to a latent state  $\mathbf{z}_t \in \mathbb{R}^{d_z}$  and a modulated INR decoder  $\mathcal{F}$  that maps query locations  $\xi$  and  $\mathbf{z}_t$  to reconstructed field values.

In the first stage, the encoder  $\mathcal{G}$  processes the sparse sensor measurements within a fixed window  $\mathbf{y}_{t-k:t}$  and outputs  $\mathbf{z}_t$ . When  $\mathcal{G}$  is instantiated as a recurrent model (e.g., LSTM/GRU), it evolves hidden states  $\mathbf{h}_i \in \mathbb{R}^{d_z}$  autoregressively, and we take the final hidden state as the latent state. Concretely,

$$\mathbf{h}_i = g(\mathbf{h}_{i-1}, \mathbf{y}_i), \quad i = t - k, \dots, t, \quad \mathbf{h}_{t-k-1} = \mathbf{0}, \quad (2)$$

where  $g$  is the recurrent update. For early times, we pad missing past observations with zeros, i.e.,  $\mathbf{y}_i = \mathbf{0}$  for  $i \leq 0$ . In general (including non-recurrent window encoders), we write  $\mathbf{z}_t = \mathcal{G}(\mathbf{y}_{t-k:t})$ .

In the second stage, the modulated INR decoder  $\mathcal{F}$  takes a query location  $\xi$  and the latent state  $\mathbf{z}_t$  and outputs the corresponding field value. Specifically, we reconstruct  $\mathbf{x}(\xi, t) \in \mathbb{R}^{d_x}$  as

$$\hat{\mathbf{x}}(\xi, t) = \mathcal{F}(\xi, \mathbf{z}_t), \quad (3)$$

where  $\mathcal{F}$  is realized as a coordinate-based INR with shared parameters and lightweight *shift modulations* (FiLM) predicted from  $\mathbf{z}_t$  by a small hypernetwork. This design supports irregular meshes and arbitrary resolutions at inference by evaluating  $\mathcal{F}$  at any set of query points.

## 2.3 Architectural Choices

**Temporal encoder  $\mathcal{G}$ .** Motivated by SHRED [7] and SHRED-ROM [8], we use an LSTM as the default temporal model. STRIDE is agnostic to this choice, and we also evaluate alternative recurrent encoders including GRU [21] and Mamba [19]. To isolate the role of recurrence, we additionally consider non-recurrent window encoders such as an MLP applied to concatenated observations and a multi-head self-attention encoder over the observation sequence.

**INR decoder  $\mathcal{F}$ .** We investigate two modulated INR backbones: SIREN [13] and FMMNN [17]. The standard SIREN architecture is defined as

$$f_\theta(\xi) = \mathbf{W}_L (\sigma_{L-1} \circ \sigma_{L-2} \circ \dots \circ \sigma_0(\xi)) + \mathbf{b}_L, \text{ with } \sigma_i(\eta_i) = \sin(\omega_0 (\mathbf{W}_i \eta_i + \mathbf{b}_i)) \quad (4)$$

where  $\theta = \{\mathbf{W}_i, \mathbf{b}_i\}_{i=0}^L$  are trainable parameters and  $\omega_0$  is a hyperparameter controlling the frequency bandwidth. To condition the INR on a latent state  $\mathbf{z}$ , we employ FiLM-style shift modulations [14], which provide a lightweight conditioning mechanism. The resulting modulated SIREN is

$$f_{\theta, \phi}(\xi) = \mathbf{W}_L (\sigma_{L-1} \circ \sigma_{L-2} \circ \dots \circ \sigma_0(\xi)) + \mathbf{b}_L, \text{ with } \sigma_i(\eta_i) = \sin(\omega_0 (\mathbf{W}_i \eta_i + \mathbf{b}_i + \phi_i)) \quad (5)$$

where  $\theta$  are shared parameters and  $\phi = \{\phi_i\}_{i=0}^{L-1}$  are shift modulations mapped from  $\mathbf{z}$  via a (typically linear) hypernetwork. We follow standard operator-learning implementations of FiLM-style modulation (e.g., 15).

The Fourier Multi-Component and Multi-Layer Neural Network (FMMNN) can serve as an INR backbone in the same manner as SIREN, while offering improved optimization behavior for high-frequency structures [17].

$$f_\theta(\xi) = \sigma_L \circ \sigma_{L-1} \circ \dots \circ \sigma_1(\xi), \text{ with } \sigma_i(\eta_i) = \mathbf{A}_i \sin(\mathbf{W}_i \eta_i + \mathbf{b}_i) + \mathbf{c}_i \quad (6)$$

where  $\{\mathbf{W}_i, \mathbf{b}_i\}$  are randomly initialized and fixed, while  $\{\mathbf{A}_i, \mathbf{c}_i\}$  are trainable. In each layer, the number of components  $d_i$  is known as the rank, and the number of hidden neurons  $n_i$  is referred to as the layer width; typically  $n_i \gg d_i$  to provide a rich set of random basis functions. To condition the network on some latent state  $\mathbf{z}$ , similar shift modulations are applied to FMMNN.

$$f_{\theta, \phi}(\xi) = \sigma_L \circ \sigma_{L-1} \circ \dots \circ \sigma_1(\xi), \text{ with } \sigma_i(\eta_i) = \mathbf{A}_i \sin(\mathbf{W}_i \eta_i + \mathbf{b}_i) + \mathbf{c}_i + \phi_i \quad (7)$$

where  $\phi = \{\phi_i\}_{i=1}^{L-1}$  are shift modulations applied to each rank, mapped from  $\mathbf{z}$  via a trainable linear hypernetwork.

To enhance the reconstruction, Fourier encoding [22] is incorporated to better capture high-frequency spatial components. Specifically, a trainable parameter matrix  $P$  is included to map the spatial coordinates to a higher-dimensional embedding  $\xi \mapsto [\xi, \cos(P\xi), \sin(P\xi)]$ , which serves as the input to the decoder.

## 2.4 Training and Normalization

We adopt an end-to-end training strategy to jointly optimize the parameters of the temporal encoder  $\mathcal{G}$  and the INR decoder  $\mathcal{F}$ . The training data consist of input-output pairs of the form  $\{\mathbf{y}_{t-k:t}, \xi, \mathbf{x}(\xi, t)\}$ , where  $\xi$  denotes query

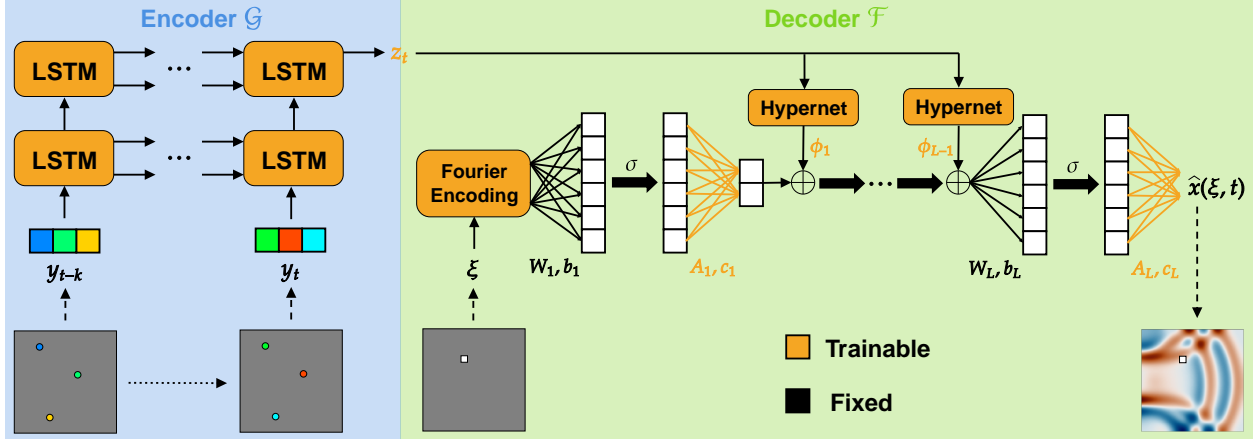


Figure 1: Overview of STRIDE. A temporal encoder maps a window of point-sensor observations  $\mathbf{y}_{t-k:t}$  to a latent state  $\mathbf{z}_t$ . A conditional spatial decoder, e.g., modulated INR decoder (FMMNN with shift modulation), then evaluates  $\hat{\mathbf{x}}(\xi, t)$  at arbitrary query locations  $\xi$  (optionally Fourier-encoded), enabling discretization- and resolution-invariant reconstruction across parameterized trajectories.

locations and  $\mathbf{x}(\xi, t)$  the corresponding ground-truth field values. We minimize the following Mean Squared Error (MSE):

$$\mathcal{L} = \frac{1}{N_{tr} N_t N_\xi} \sum_{j=1}^{N_{tr}} \sum_{t=1}^{N_t} \sum_{q=1}^{N_\xi} \left\| \mathbf{x}(\xi_{j,t}^{(q)}, t; \boldsymbol{\mu}_j) - \hat{\mathbf{x}}(\xi_{j,t}^{(q)}, t; \boldsymbol{\mu}_j) \right\|^2, \quad (8)$$

where  $j$  indexes training trajectories generated at parameters  $\{\boldsymbol{\mu}_j\}_{j=1}^{N_{tr}}$  and  $N_t$  is the number of time steps per trajectory. For each snapshot  $(j, t)$ , we sample  $N_\xi$  query points  $\{\xi_{j,t}^{(q)}\}_{q=1}^{N_\xi}$  from the available spatial discretization (or directly from  $\Omega$ ) and compute predictions via  $\hat{\mathbf{x}}(\xi, t, \boldsymbol{\mu}_j) = \mathcal{F}(\xi, \mathcal{G}(\mathbf{y}_{t-k:t}(\boldsymbol{\mu}_j)))$ . Unlike SHRED, which matches full spatial grids at each step, randomized spatial sampling reduces training cost and directly enables discretization- and resolution-invariant learning. To facilitate fast and stable training, we use the SOAP optimizer [23] with weight decay, along with the ReduceLROnPlateau scheduler.

Prior to training, we perform channel-wise normalization similar to [24]. Specifically, we scale the state variables  $\mathbf{x}$  (and thus the sensor measurements  $\mathbf{y}$ ) and the spatial coordinates  $\xi$  such that each component resides within the range  $[-1, 1]$ . This normalization helps improve numerical stability, especially for early-time snapshots and boundary regions that may contain many near-zero values.

### 3 Theoretical Justification

We provide a conditional justification for why reconstructing the full field from a *finite* window of point sensors is plausible, and why a two-stage architecture (temporal encoder + spatial decoder) is expressive enough to approximate the associated reconstruction operator.

#### 3.1 Setting

Let  $\Omega \subset \mathbb{R}^{d_\xi}$  be a compact spatial domain and let  $d_x$  be the number of field channels. Consistent with Section 2, we denote the full state at discrete time index  $t$  by the vector-valued field  $\mathbf{x}_t(\cdot) \in X$ , and write its pointwise value as  $\mathbf{x}(\xi, t) := \mathbf{x}_t(\xi) \in \mathbb{R}^{d_x}$ . We make the dependence on the parameter explicit by  $\mathbf{x}_t(\cdot; \boldsymbol{\mu})$  and  $\mathbf{x}(\xi, t; \boldsymbol{\mu})$ . Here  $X$  is a Banach space continuously embedded in  $C^0(\Omega, \mathbb{R}^{d_x})$  so that point evaluation is continuous, e.g.,  $X = H^s(\Omega, \mathbb{R}^{d_x})$  with  $s > d_\xi/2$  by Sobolev embedding.

In our numerical benchmarks, trajectories arise from a *parametric* PDE: there is a compact parameter set  $\mathcal{P} \subset \mathbb{R}^{d_\mu}$  and each trajectory is generated under some fixed  $\boldsymbol{\mu} \in \mathcal{P}$  (e.g., geometry/forcing/initial-condition parameters). Let  $\{S_\mu^t\}_{t \geq 0}$  be the (semi)flow on  $X$  induced by the PDE at parameter  $\boldsymbol{\mu}$ , and fix a sampling interval  $\Delta t > 0$  with discrete-time map  $F_\mu := S_\mu^{\Delta t}$ . Thus, for a fixed  $\boldsymbol{\mu}$ ,  $\mathbf{x}_{t+1} = F_\mu \mathbf{x}_t$  for integer  $t \geq 0$ . We assume that for each  $\boldsymbol{\mu} \in \mathcal{P}$  the dynamics admit a compact forward-invariant set  $\mathcal{A}_\mu \subset X$  (e.g., a parameter-dependent global attractor in dissipative settings) on

which the solution map is regular enough for delay embedding arguments. To unify multiple-trajectory learning across parameters, we consider the augmented invariant set in  $\mathcal{P} \times X$ ,

$$\mathcal{A} := \{(\boldsymbol{\mu}, \mathbf{x}) : \boldsymbol{\mu} \in \mathcal{P}, \mathbf{x} \in \mathcal{A}_{\boldsymbol{\mu}}\} \subset \mathcal{P} \times X, \quad (9)$$

equipped with the product norm  $\|(\boldsymbol{\mu}, \mathbf{x}) - (\boldsymbol{\mu}', \mathbf{x}')\|_{\mathcal{P} \times X} := \|\boldsymbol{\mu} - \boldsymbol{\mu}'\| + \|\mathbf{x} - \mathbf{x}'\|_X$ .

### 3.2 Point-sensor observation and delay observability

Fix  $N_s$  sensor locations  $\{\boldsymbol{\xi}^{(1)}, \dots, \boldsymbol{\xi}^{(N_s)}\} \subset \Omega$  and let  $d_o$  denote the number of observed channels at each sensor, so the observation dimension is  $p = N_s \times d_o$ . Let  $\Pi : \mathbb{R}^{d_x} \rightarrow \mathbb{R}^{d_o}$  be the fixed linear projection selecting the observed channels. Define the point-sensor map  $h : X \rightarrow \mathbb{R}^p$  by stacking projected sensor values as

$$h(\mathbf{x}) = (\Pi \mathbf{x}(\boldsymbol{\xi}^{(1)}), \dots, \Pi \mathbf{x}(\boldsymbol{\xi}^{(N_s)})) \in \mathbb{R}^p. \quad (10)$$

For an integer lag  $k \geq 0$ , define the *forward* delay map  $\Phi_k : \mathcal{A} \rightarrow \mathbb{R}^{(k+1)p}$  on the augmented state by

$$\Phi_k(\boldsymbol{\mu}, \mathbf{x}) = (h(\mathbf{x}), h(F_{\boldsymbol{\mu}} \mathbf{x}), \dots, h(F_{\boldsymbol{\mu}}^k \mathbf{x})). \quad (11)$$

In data terms, for a trajectory generated under a fixed  $\boldsymbol{\mu}$ ,  $\mathbf{x}_t = F_{\boldsymbol{\mu}}^t \mathbf{x}_0$  (with integer time index), define the per-step sensor vector  $\mathbf{y}_t := h(\mathbf{x}_t) \in \mathbb{R}^p$ . Then the observation window  $\mathbf{y}_{t-k:t}$  equals  $\Phi_k(\boldsymbol{\mu}, \mathbf{x}_{t-k})$ .

**Assumption 3.1** (Finite-dimensional long-term complexity). The augmented invariant set  $\mathcal{A} \subset \mathcal{P} \times X$  is compact and has finite box-counting dimension  $d_A := \dim_B(\mathcal{A}) < \infty$ .

Assumption 3.1 is satisfied by broad classes of *dissipative* PDEs for which the solution (semi)flow possesses a compact global attractor with finite fractal/box-counting dimension; classical examples include the 1D Kuramoto–Sivashinsky equation, the 2D Navier–Stokes equations, and geophysical flows (see, e.g., 25). In our benchmarks, the KS, FlowAO, and SWE settings are dissipative, and the seismic-wave setup includes an absorbing damping mask that introduces dissipation in the simulated dynamics. Moreover, our datasets are parametric: varying  $\boldsymbol{\mu}$  (e.g., forcing/geometry profiles, initial conditions, source location, velocity map) traces out a *family* of invariant sets  $\{\mathcal{A}_{\boldsymbol{\mu}}\}_{\boldsymbol{\mu} \in \mathcal{P}}$ ; Assumption 3.1 asserts that the resulting augmented set  $\mathcal{A} \subset \mathcal{P} \times X$  remains effectively finite-dimensional.

**Assumption 3.2** (Stable delay observability). There exist a lag  $k$  and constants  $L_{\Phi}, L_{\Psi} > 0$  such that  $\Phi_k$  is injective on  $\mathcal{A}$  and has an inverse  $\Psi : Y \rightarrow \mathcal{A}$  on  $Y := \Phi_k(\mathcal{A})$  satisfying the bi-Lipschitz-type stability bounds

$$\|\Phi_k(\mathbf{a}) - \Phi_k(\mathbf{a}')\| \leq L_{\Phi} \|\mathbf{a} - \mathbf{a}'\|_{\mathcal{P} \times X}, \quad (12)$$

with  $\mathbf{a} = (\boldsymbol{\mu}, \mathbf{x})$  and  $\mathbf{a}' = (\boldsymbol{\mu}', \mathbf{x}')$  and

$$\|\Psi(\mathbf{y}) - \Psi(\mathbf{y}')\|_{\mathcal{P} \times X} \leq L_{\Psi} \|\mathbf{y} - \mathbf{y}'\|. \quad (13)$$

Equivalently, the inverse is continuous and stable to perturbations of the observation window.

Assumption 3.2 is a *stable* observability/embedding condition for the delay-coordinate map on the augmented set  $\mathcal{A}$ . For infinite-dimensional systems such as dissipative PDEs, the Mañé projection theorem shows that compact sets of finite box-counting dimension in Banach spaces admit injective linear projections into  $\mathbb{R}^{d_z}$  (with Hölder continuous inverse) when  $d_z$  is sufficiently large [20]. In our setting,  $h$  is a fixed *point-sensor* map and does not directly observe  $\boldsymbol{\mu}$ , so genericity is not automatic; we therefore treat Assumption 3.2 as an identifiability assumption on  $(\boldsymbol{\mu}, \mathbf{x})$  and empirically examine parameter identification.

### 3.3 A continuous reconstruction operator

Define the (ground-truth) field at time index  $t$  as  $\mathbf{x}(\cdot, t) := \mathbf{x}_t(\cdot) \in C^0(\Omega, \mathbb{R}^{d_x})$ . Under Assumption 3.2, an observation window  $\mathbf{y} \in Y$  identifies the corresponding augmented state  $(\boldsymbol{\mu}, \mathbf{x}) = \Psi(\mathbf{y}) \in \mathcal{A}$  at the *start* of the window. The field at the end of the window is then  $F_{\boldsymbol{\mu}}^k \mathbf{x}$ . This defines the reconstruction operator  $T : Y \rightarrow C^0(\Omega, \mathbb{R}^{d_x})$ :

$$T(\mathbf{y})(\boldsymbol{\xi}) := (F_{\boldsymbol{\mu}}^k \mathbf{x})(\boldsymbol{\xi}), \quad \mathbf{y} \in Y, \boldsymbol{\xi} \in \Omega. \quad (14)$$

**Lemma 3.3** (Continuity and stability of  $T$ ). *If the map  $(\boldsymbol{\mu}, \mathbf{x}) \mapsto F_{\boldsymbol{\mu}}^k \mathbf{x}$  is continuous on  $\mathcal{A}$  and point evaluation  $\mathbf{x} \mapsto \mathbf{x}(\boldsymbol{\xi})$  is continuous on  $X$ , then  $T$  is continuous on the compact set  $Y$ . Moreover, if  $(\boldsymbol{\mu}, \mathbf{x}) \mapsto F_{\boldsymbol{\mu}}^k \mathbf{x}$  is  $L_{F^k}$ -Lipschitz on  $\mathcal{A}$  (with respect to  $\|\cdot\|_{\mathcal{P} \times X}$ ) and the embedding  $X \hookrightarrow C^0(\Omega, \mathbb{R}^{d_x})$  satisfies  $\|\mathbf{x}\|_{C^0} := \sup_{\boldsymbol{\xi} \in \Omega} \|\mathbf{x}(\boldsymbol{\xi})\| \leq C_{\text{ev}} \|\mathbf{x}\|_X$ ,  $\forall \mathbf{x} \in X$ , then*

$$\sup_{\boldsymbol{\xi} \in \Omega} \|T(\mathbf{y})(\boldsymbol{\xi}) - T(\mathbf{y}')(\boldsymbol{\xi})\| \leq C_{\text{ev}} L_{F^k} L_{\Psi} \|\mathbf{y} - \mathbf{y}'\|. \quad (15)$$

We provide the proof in Appendix A.1. Stable delay observability implies that small perturbations of the sensor window (noise, discretization) induce controlled reconstruction errors.

### 3.4 Approximation by a STRIDE-type architecture

We now connect the operator  $T$  to STRIDE's structure. Let  $\mathcal{G} : Y \rightarrow Z$  be a temporal encoder that maps observation windows to a latent state  $z \in Z$ , and let  $\mathcal{F} : \Omega \times Z \rightarrow \mathbb{R}^{d_x}$  be a conditional spatial decoder. STRIDE represents reconstructions as  $\hat{x}(\xi) = \mathcal{F}(\xi, \mathcal{G}(y))$ .

**Theorem 3.4** (Operator factorization and approximation). *Assume Assumptions 3.1–3.2 and that  $G_k(\mu, x) := F_\mu^k x$  is continuous on  $\mathcal{A}$ . Let  $\mathcal{A}_X$  be the projection of  $\mathcal{A}$  onto  $X$  and set  $d_X := \dim_B(\mathcal{A}_X)$ . Then there exists a compact set  $Z \subset \mathbb{R}^{d_z}$  with  $d_z > 2d_X$  and continuous maps  $\mathcal{G} : Y \rightarrow Z$  and  $\mathcal{F} : \Omega \times Z \rightarrow \mathbb{R}^{d_x}$  of STRIDE form such that*

$$\sup_{y \in Y} \sup_{\xi \in \Omega} \|T(y)(\xi) - \mathcal{F}(\xi, \mathcal{G}(y))\| < \varepsilon, \quad (16)$$

where  $\mathcal{G}$  and  $\mathcal{F}$  can be uniformly approximated on compact sets by standard feedforward neural networks.

The proof is provided in Appendix A.2. Though the formal approximation guaranty is for standard feedforward networks, in practice, we instantiate  $\mathcal{G}$  with a windowed recurrent encoder and  $\mathcal{F}$  with a modulated INR; these architectures are more expressive in our experiments.

## 4 Experiments

We evaluate STRIDE on four benchmarks that reconstruct spatiotemporal fields from sparse point-sensor observations. The benchmarks range from chaotic dynamics to wave propagation and all involve multiple trajectories driven by varying initial conditions and/or physical parameters. In this section, we denote STRIDE-FMMNN as our default instantiation with an FMMNN INR backbone and STRIDE-SIREN as the SIREN-backbone variant.

### 4.1 Experimental Setup

**Kuramoto–Sivashinsky Equation.** The Kuramoto–Sivashinsky (KS) equation is a nonlinear PDE that exhibits spatiotemporal chaos and strong sensitivity to initial conditions, as illustrated in Fig. 2, where the system exhibits divergent dynamics despite starting from nearly identical initial conditions. Following [8], we generate data using the Exponential Time Differencing fourth-order Runge–Kutta (ETDRK4) method with periodic boundary conditions on  $N_\xi = 100$  spatial points for  $N_t = 201$  snapshots. We fix the viscosity to 1.0 and vary only the initial condition, generating 1,000 trajectories.

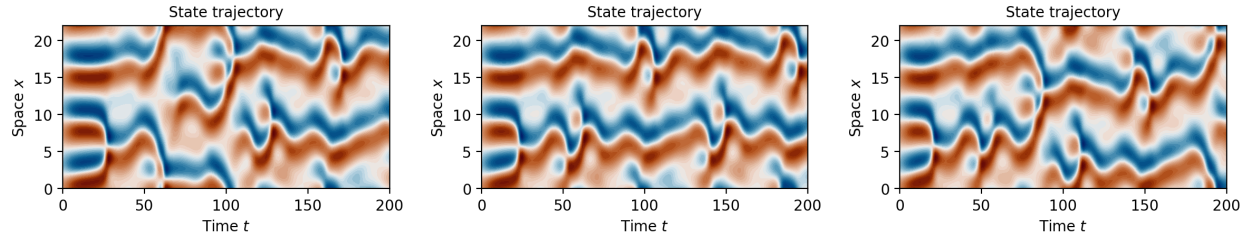


Figure 2: Divergent trajectories in the chaotic KS system. The spatiotemporal fields are initialized with nearly identical frequency parameters (2.99, 3.00, and 3.01), illustrating the system's sensitive dependence on initial conditions.

**Flow Around an Obstacle.** Flow Around an Obstacle (FlowAO) is an incompressible flow benchmark with time-dependent physical and geometric parameters. Following [8], we generate 200 trajectories with  $N_t = 200$  time steps each by solving the unsteady Navier–Stokes equations. Each trajectory corresponds to a different time profile of the angle of attack and inflow intensity, as well as a different obstacle shape; see one example trajectory in Fig. 3. Each snapshot contains  $N_\xi = 40,296$  spatial points per velocity component.

**Shallow Water Equations.** The shallow water equations (SWE) model free-surface flow, e.g., as used in tsunami modeling shown in Fig. 4. We generate 200 trajectories with  $N_t = 201$  time steps, initialized with Gaussian bumps of surface elevation at random locations, following [26]. The spatial domain is discretized uniformly at two resolutions:  $64 \times 64$  and  $128 \times 128$ .

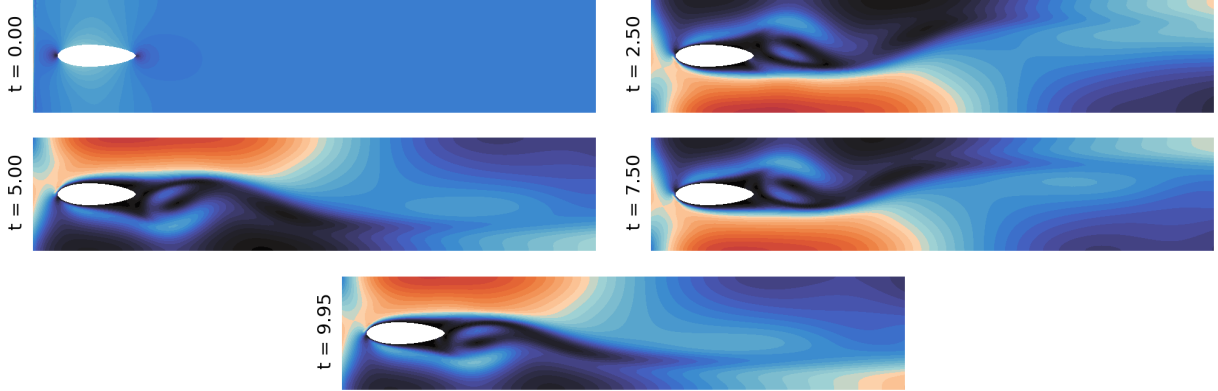


Figure 3: Example trajectory of the velocity field in the FlowAO case, showing unsteady flow patterns influenced by time-varying angles of attack and inflow intensities.

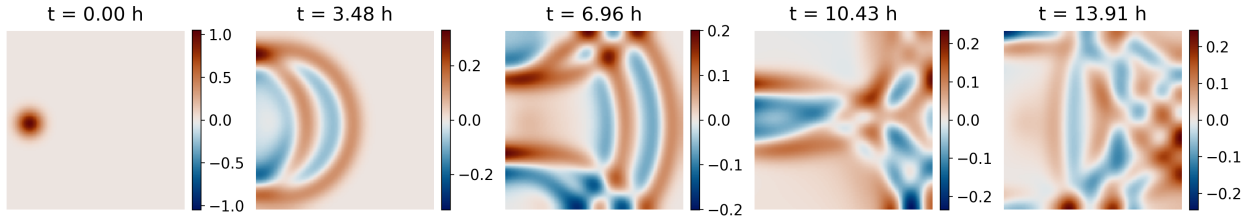


Figure 4: Example trajectory of the surface elevation in the SWE case, demonstrating the propagation of a tsunami-like wave generated from a Gaussian source.

**Seismic Wave Propagation.** We consider wavefields governed by the acoustic wave equation. Using Devito [27], we generate 1,000 trajectories with  $N_t = 201$  time steps, where a 10 Hz Ricker source is placed at random locations in a multi-layer velocity map sourced from the ‘‘FlatVel-B’’ (FVB) dataset from OpenFWI [28], see one sample in Fig. 5. The spatial resolution is  $70 \times 70$ , with an absorbing damping mask applied at the domain boundaries to mimic an infinite domain. Layer boundaries induce complex wave phenomena, including refraction and reflection, thereby significantly complicating the reconstruction task. One example of the wave propagation is shown in Fig. 6.

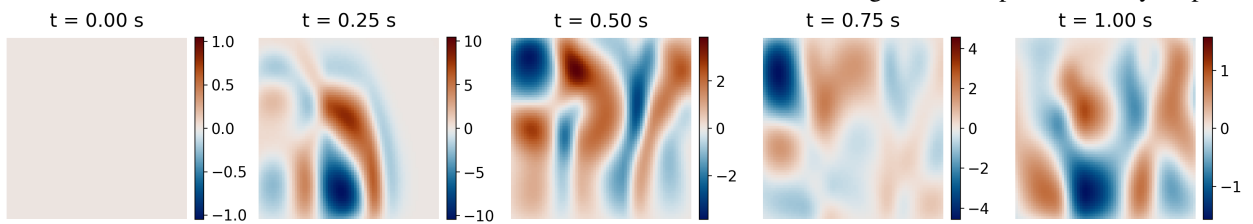
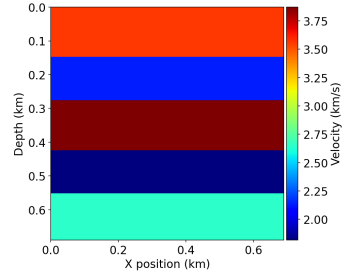


Figure 6: Example trajectory of acoustic wave propagation across a multi-layer velocity map, illustrating complex reflections and refractions.

## 4.2 Evaluation Metrics

The generated trajectories are partitioned into 80%/10%/10% splits for training, validation, and testing. During training and validation, we may subsample spatial query points as described in Section 2; at test time, we evaluate reconstructions on all available spatial points. For the KS and FlowAO cases, we

report the mean relative  $\ell_2$  error for each state variable,

$$\epsilon = \frac{1}{N_{\text{test}} N_t} \sum_{j=1}^{N_{\text{test}}} \sum_{t=1}^{N_t} \frac{\|\mathbf{x}_{j,t} - \hat{\mathbf{x}}_{j,t}\|_2}{\|\mathbf{x}_{j,t}\|_2}, \quad (17)$$

where  $\|\cdot\|_2$  is the Euclidean norm over the spatial discretization and  $N_{\text{test}}$  is the number of test trajectories. Due to the wide dynamic range of the wavefields, we report the following overall relative Frobenius error for the SWE and Seismic cases,

$$\epsilon = \frac{\|\mathbf{x} - \hat{\mathbf{x}}\|_F}{\|\mathbf{x}\|_F}, \quad (18)$$

where  $\mathbf{x}$  and  $\hat{\mathbf{x}}$  are matrices formed by stacking the true and predicted spatial fields (over time and space) of the test samples.

### 4.3 Numerical Results

Table 1 summarizes reconstruction errors and parameter counts for our method and baselines across the four datasets. STRIDE-SIREN uses the same STRIDE architecture but replaces the INR backbone with a modulated SIREN. For FlowAO, we observe only the horizontal velocity component at sensor locations and reconstruct both velocity components; we report the error of the horizontal component. For SWE, we observe only the surface elevation and reconstruct the elevation and both velocity components; we report the error of the surface elevation. For STRIDE-FMMNN, we report parameters as (trainable/all) due to fixed random weights in FMMNN. Model hyperparameters are selected using Bayesian optimization on the validation set. To ensure a fair comparison of the decoder, all models use the same sensor measurements, time lag  $k$ , and latent dimension  $d_z$ . Please refer to Appendix B for details on hyperparameter search and training.

STRIDE-FMMNN achieves the lowest errors across all datasets. SHRED performs well on KS but degrades as the spatial dimensionality increases, since the parameter count is dominated by the last layer of its shallow decoder and scales with the output dimension. SHRED-ROM reduces parameters via Proper Orthogonal Decomposition (POD) but incurs larger errors in intrinsically high-dimensional systems. Across the four datasets, POD achieves mean relative reconstruction errors of 0.57%, 0.45%, 0.80%, and 1.47% on the test sets, employing 20, 150, 400, and 2000 modes, respectively. STRIDE-SIREN is a competitive baseline, but is consistently outperformed by STRIDE-FMMNN at comparable model sizes, especially in wave propagation problems.

Table 1: Model comparison of parameter count and reconstruction error ( $\epsilon$ ) per dataset.

MODEL	DATASET →	KS	FlowAO	SWE (128×128)	Seismic
SHRED	#PARAMETERS	425K	32.5M	20.1M	3.09M
	ERROR $\epsilon$	<u>6.20E-2</u>	4.13E-2	1.75E-1	1.67E-1
SHRED-ROM	#PARAMETERS	393K	395K	917K	1.93M
	ERROR $\epsilon$	6.28E-2	6.53E-2	5.14E-1	4.87E-1
STRIDE-SIREN	#PARAMETERS	448K	121K	397K	1.49M
	ERROR $\epsilon$	6.34E-2	<u>3.12E-2</u>	<u>4.62E-2</u>	<u>1.12E-1</u>
STRIDE-FMMNN	#PARAMETERS	348K/484K	103K/149K	337K/407K	1.39M/1.80M
	ERROR $\epsilon$	<b>3.09E-2</b>	<b>2.97E-2</b>	<b>2.78E-2</b>	<b>8.41E-2</b>

The comparison among different models holds for a more challenging SWE variant. As shown in Table 2, STRIDE-FMMNN remains the best-performing model when we double the simulated physical time (while keeping  $N_t = 201$ ) so that wave reflections introduce more complexity near the end of the trajectories.

Table 2: Model comparison of parameters and error on the extended SWE (128×128) dataset.

MODEL	SHRED	SHRED-ROM	STRIDE-SIREN	STRIDE-FMMNN
#PARAMETERS	20.1M	917K	1.45M	918K/1.53M
ERROR $\epsilon$	20.25%	57.09%	2.89%	<b>2.51%</b>

Fig. 7 compares STRIDE-FMMNN and the baselines on a test snapshot from extended (double in time) SWE ( $128 \times 128$ ). As waves bounce back and forth in the physical domain, the surface elevation field  $\eta$  becomes highly structured near the final time step. Given the same sparse observations, STRIDE-FMMNN substantially improves reconstruction accuracy over SHRED and STRIDE-SIREN.

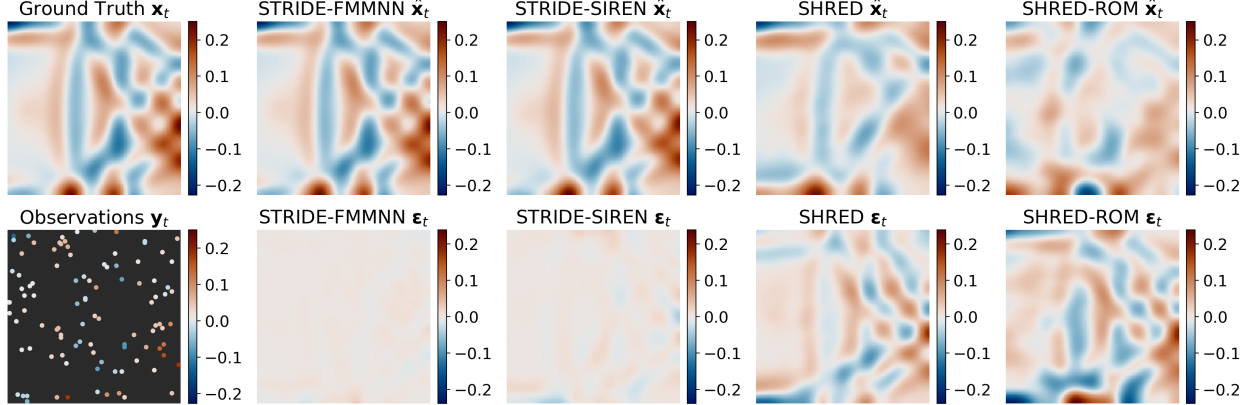


Figure 7: Visualization of the surface elevation  $\eta$  in the extended SWE ( $128 \times 128$ ) case. The first column shows the ground truth at the last (200th) time step in an example test trajectory, along with observations at 100 random locations used as model input. The next columns show the prediction and error of STRIDE-FMMNN and baseline models for the same snapshot.

Fig. 8 provides a visual comparison between STRIDE-FMMNN and baseline models for a representative test snapshot from the Seismic dataset. The superiority of the proposed framework is particularly evident at the final time step, where the wavefield develops highly complex interference patterns resulting from cumulative refraction and reflection across multi-layered media.

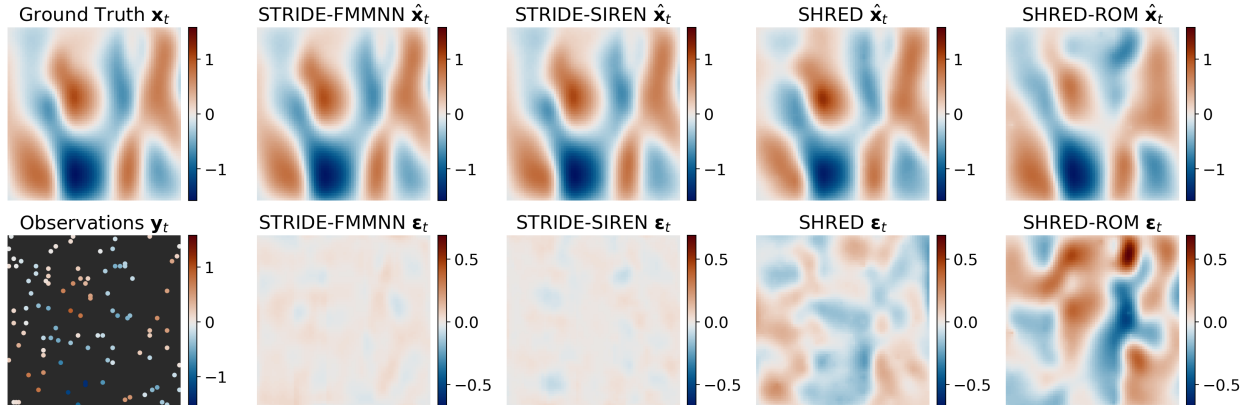


Figure 8: Visual comparison of acoustic wave reconstruction under complex interference. (Left) Ground truth at  $t = 200$  with 100 random sparse observations. (Right) Predicted wavefields and corresponding error maps for STRIDE-FMMNN and baselines, highlighting our model’s ability to capture intricate reflection and refraction patterns.

As shown in Fig. 9, STRIDE-FMMNN outperforms SHRED, STRIDE-SIREN, and SHRED-ROM at each time step for the KS and SWE cases. While all models exhibit larger errors at early times (limited history), STRIDE-FMMNN maintains a lower error as predictions become more challenging in chaotic dynamics (KS) and as spatial fields become increasingly complex (SWE).

Fig. 10 shows representative latent state trajectories produced by STRIDE-FMMNN on FlowAO and Seismic. In FlowAO, the latent states exhibit clear periodic behavior after the initial burn-in (time lag  $k$ ), consistent with periodic wake dynamics. In Seismic, the latent magnitude decays over time, matching the attenuation of the wavefield as it reaches the boundaries and is absorbed by the damping mask.

Beyond improved accuracy, STRIDE-FMMNN supports discretization- and resolution-invariant training via coordinate-based decoding and randomized spatial sampling. We consider a more challenging scenario where the standard deviation

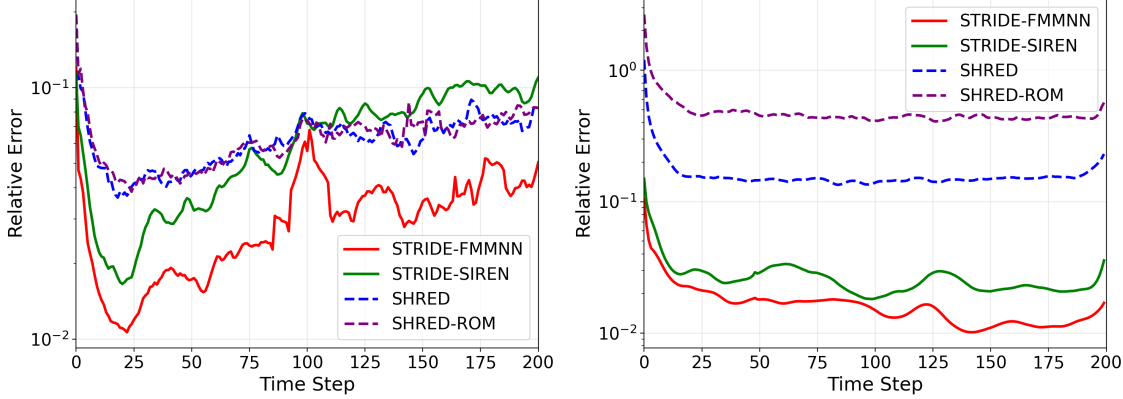


Figure 9: Mean relative prediction error along test trajectories for the KS (left) and SWE (128×128) (right) cases, comparing STRIDE-FMMNN and STRIDE-SIREN with baselines.

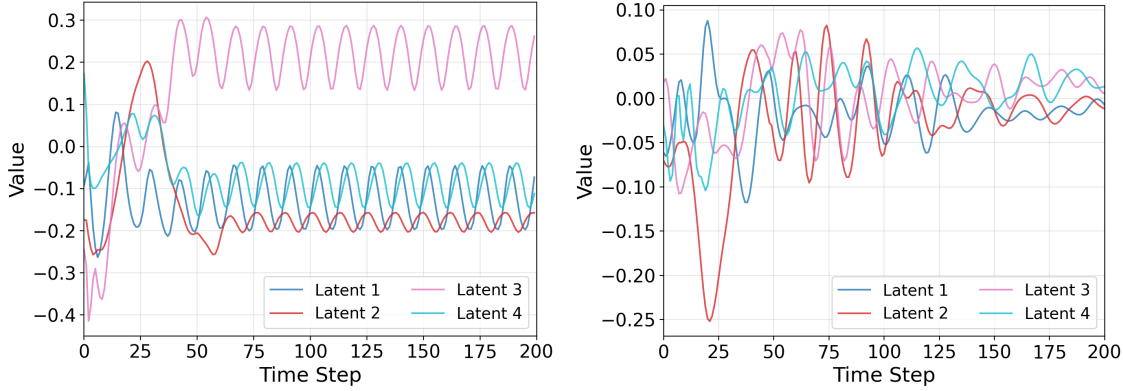


Figure 10: The first four latent states of STRIDE-FMMNN in an example test trajectory for the FlowAO (left) and Seismic (right) cases.

of the initial Gaussian bump is halved, effectively doubling the characteristic frequency of the wavefield. Here, we generate low-resolution data by downsampling the high-resolution simulation data, and arrange the sensors on a uniform grid to ensure consistent evaluation. As shown in Table 3, STRIDE-FMMNN achieves consistent performance across resolutions in standard settings, provided the model size and training budget (fixed at  $N_\xi = 4,096$  query points per snapshot) remain constant. In super-resolution settings (training at low resolution and testing at higher resolution), STRIDE-FMMNN maintains similar errors without retraining. Specifically, when super-resolving from 64 to 128, the relative errors are comparable to those obtained by training directly on the 128-resolution dataset. Furthermore, this approach significantly outperforms baseline methods that rely on bilinear interpolation to upsample low-resolution predictions.

Table 3: Comparison of STRIDE-FMMNN prediction errors (%) against interpolation baselines for the extended high-frequency SWE case on standard and super-resolution tasks.

VAR.	STANDARD		SUPER-RES	INTERP.
	64	128	64 → 128	64 → 128
$u$	6.89	7.02	6.97	8.02
$v$	5.15	5.03	5.29	6.66
$\eta$	6.27	6.57	6.32	7.57

The FMMNN backbone in STRIDE-FMMNN yields more stable optimization and faster convergence than STRIDE-SIREN. Fig. 11 visualizes the training dynamics of three runs with STRIDE-FMMNN and STRIDE-SIREN under comparable model sizes and identical optimizer/scheduler settings. With a learning rate of 2e-3, STRIDE-FMMNN

converges within 300 epochs, while STRIDE-SIREN converges (by validation loss) in about 700 epochs with a learning rate of 1e-4. With a larger learning rate for STRIDE-SIREN (e.g., 2e-4), we observe an early spike that leads to non-convergence. Finally, STRIDE-FMMNN exhibits higher training loss but lower validation loss at convergence, suggesting reduced overfitting due to its low-rank, partially trainable parameterization.

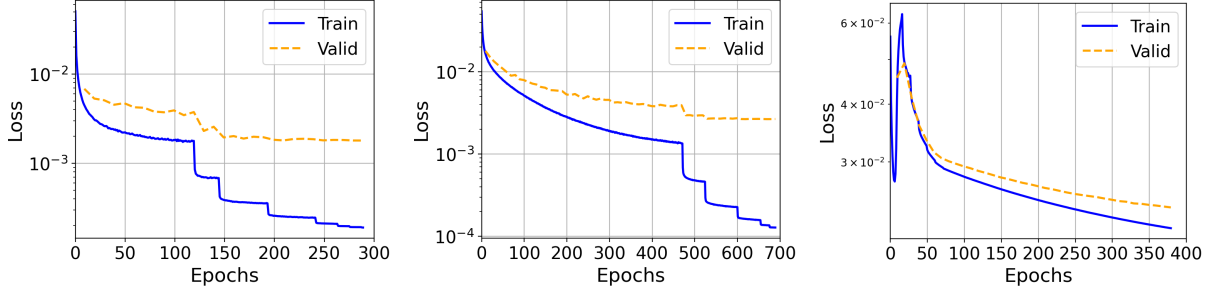


Figure 11: Training dynamics of STRIDE-FMMNN (left) and STRIDE-SIREN (middle and right) for the KS case. The three trainings use the same optimizer and scheduler, with learning rates set to 2e-3, 1e-4, and 2e-4, respectively.

Fig. 12 shows the impact of time lag and number of random sensors on the overall relative error of STRIDE-FMMNN on the SWE (128×128) dataset. Empirically, the relative error decreases with longer time lags and more random sensors. This validates the choice of time lag and number of sensors as discussed in Section 3.

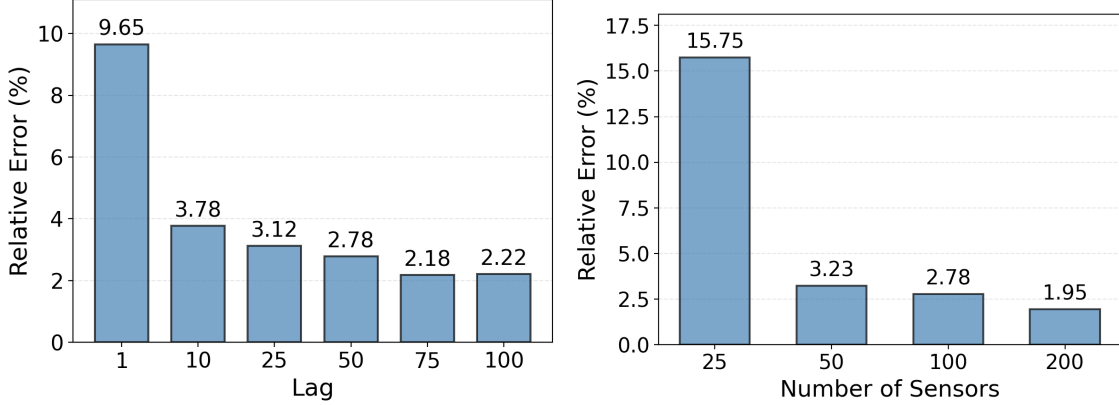


Figure 12: Ablation studies of STRIDE-FMMNN across time lags and the number of sensors on the SWE (128×128) dataset.

Table 4 evaluates the robustness of STRIDE-FMMNN against different observation noise levels. We define the noise level as the standard deviation of the applied Gaussian noise relative to the standard deviation of the true observations. The results demonstrate the framework’s robustness, yielding a remarkably low prediction error of 6.24% under a high noise condition of 20%.

Table 4: STRIDE-FMMNN prediction errors (%) for  $\eta$  with different observation noise levels (%)

NOISE LEVEL	0	5	10	20
ERROR	2.78	3.22	4.04	6.24

We compare different temporal encoders within STRIDE-FMMNN, using a fixed latent dimension and the same FMMNN decoder. The left panel of Fig. 13 shows that recurrent models (LSTM, GRU, and Mamba) substantially outperform MLP and self-attention variants in both accuracy and parameter efficiency. Mamba achieves the lowest prediction error with a model size comparable to LSTM. The right panel summarizes LSTM vs. Mamba across datasets: Mamba slightly outperforms LSTM in most cases with KS as an exception. This suggests that Mamba is a promising temporal encoder for extracting latent states.

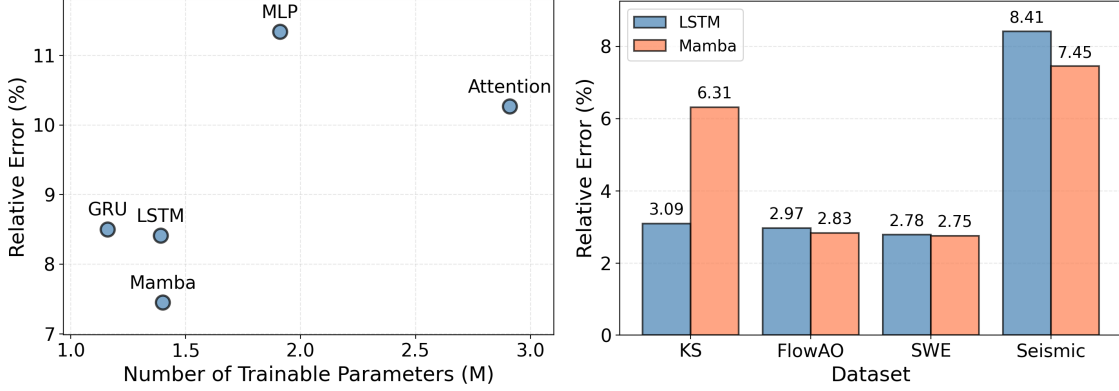


Figure 13: Comparison of temporal models on the Seismic dataset (left) and prediction errors using LSTM or Mamba per dataset (right).

Fig. 14 demonstrates the performance of STRIDE-FMMNN on both in-distribution and out-of-distribution (OOD) samples for the SWE case. When test samples are drawn within the training range, the proposed model achieves very low relative errors as previously reported. However, generalizing to unseen scenarios remains a significant challenge, even when the dynamics are simply flipped in the OOD samples. Prediction errors remain below 10% only when the test samples are fairly close to the training range. For samples further outside this distribution, relative errors easily exceed 30%.

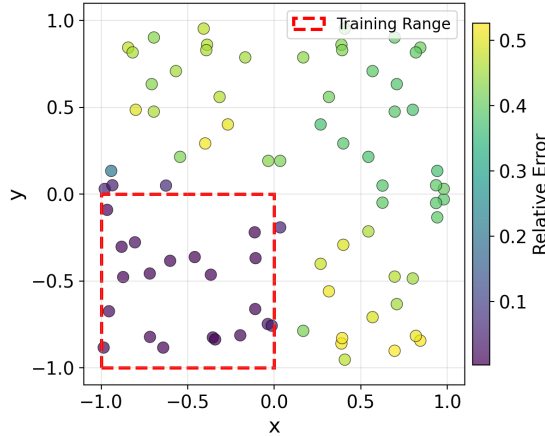


Figure 14: Generalization analysis of STRIDE-FMMNN on the SWE dataset. The scatter plot displays the relative prediction error for surface elevation ( $\eta$ ) across in-distribution and out-of-distribution samples. The coordinates of each point correspond to the center of the initial Gaussian bump. Training trajectories are exclusively initialized within the lower-left quarter.

In addition to full-field reconstruction, the underlying control parameters can be accurately estimated from the informative latent states learned by STRIDE-FMMNN using a simple MLP. As illustrated in Fig. 15, the estimated parameters for the SWE and FlowAO cases closely match the ground truth in an example test trajectory. Among all the test trajectories, the mean absolute errors for the two parameters defining the location of the initial Gaussian bump (sampled from  $[-1, 0] \times [-1, 0]$ ) are **1.47e-3** and **8.33e-4**. The mean absolute error of the time-varying angle of attack is **2.10e-2**.

Fig. 16 shows the performance of auto-regressive forecasting using STRIDE-FMMNN. To extend the framework for future-state prediction, we train an auxiliary LSTM network on the time series of learned latent states. This enables the extrapolation of future latent trajectories, which are subsequently mapped back to full spatial fields via the pre-trained FMMNN decoder. In the SWE case, the model demonstrates robust short-term forecasting capabilities, maintaining relative errors of approximately 25% across all three state variables after a horizon of 21 time steps. However, the Seismic case proves significantly more challenging. The forecasting error blows up quickly and approaches 100% over the same 21-step interval.

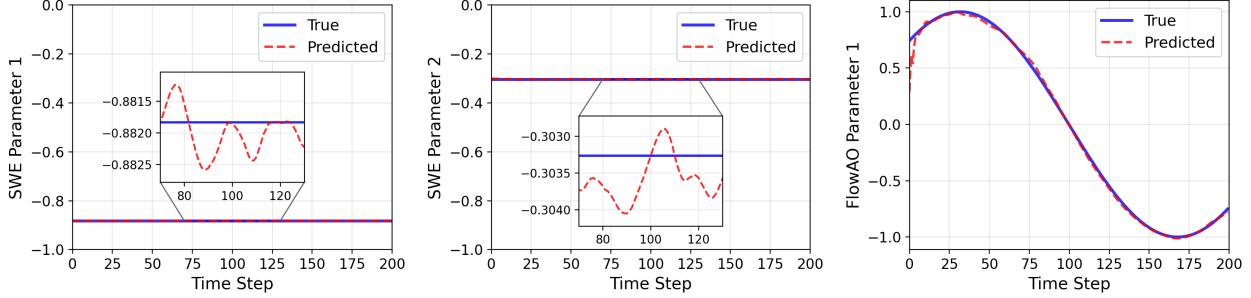


Figure 15: Parameter estimation from STRIDE-FMMNN learned latent states. Left and Middle: Estimation of the initial Gaussian bump coordinates ( $x$ - and  $y$ -locations) in an example test trajectory for the SWE case. Right: Estimation of the time-varying angle of attack for the FlowAO case.

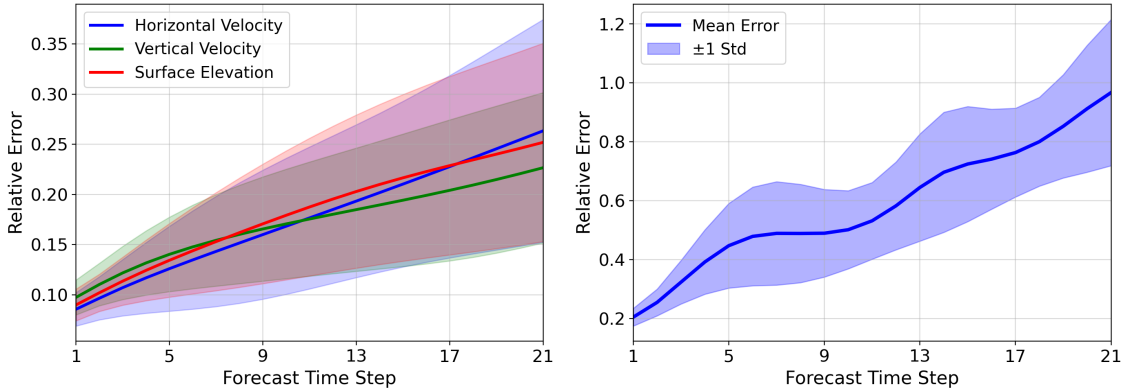


Figure 16: Auto-regressive forecasting performance of STRIDE-FMMNN. The plots illustrate the temporal evolution of relative prediction error for the SWE (left) and Seismic (right) cases. The shaded regions denote the standard deviation across all test trajectories.

The performance of the proposed framework also depends on sensor placement, especially when observations are extremely sparse. As shown in Fig. 17, we trained STRIDE-FMMNN for the SWE case with 25 sensors arranged according to three different strategies. Here, QR refers to the SSPOR algorithm implemented in PySensors [29], which utilizes QR optimization by default. The three configurations yielded overall relative errors for  $\eta$  of **15.75%**, **16.28%**, and **6.49%**, respectively. These findings underscore the critical role of data-driven sensor placement in minimizing reconstruction error. Notably, QR placement achieves the lowest error by concentrating sensors in the lower left quarter, where the Gaussian bump is initialized, thereby capturing more information about the underlying dynamics.

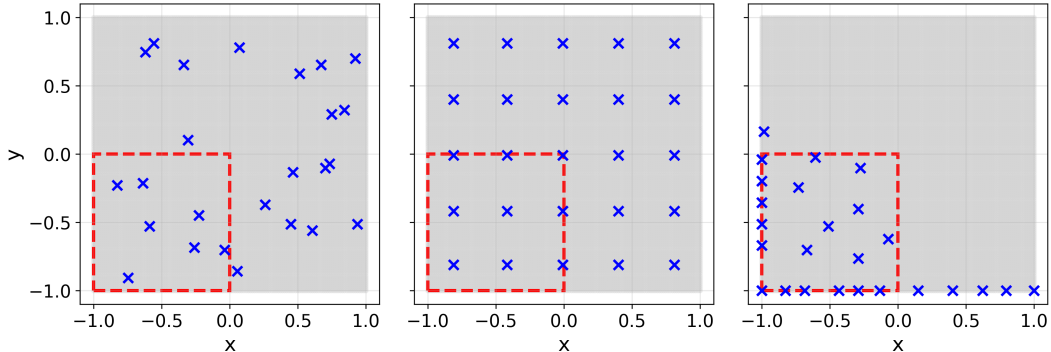


Figure 17: Comparison of sparse sensor placement strategies in the SWE domain: random (left), uniform (middle), and QR (right). The relative prediction errors for  $\eta$  with the three placement strategies are 15.75%, 16.28%, and 6.49%, respectively.

#### 4.4 Further Discussion

STRIDE inherits the computational trade-offs of INR-based decoders. Training requires backpropagation through a comparatively deep coordinate-to-field network and repeated evaluation of the decoder at many query coordinates (even when we subsample spatial points during training). At inference time, reconstructing a full field requires querying the decoder at all spatial points, so the runtime scales (approximately) linearly with the output resolution; in contrast, SHRED and SHRED-ROM output the full field (or low-dimensional coefficients) with a single forward pass. Table 5 shows that both STRIDE-FMMNN and STRIDE-SIREN incur substantially higher evaluation costs than the non-INR baselines, and they can also be slower to train depending on the spatial resolution and the decoder backbone. Training and evaluation are performed on a single NVIDIA L40S GPU.

Table 5: Model comparison of training and evaluation time per dataset. STRIDE-FMMNN uses the FMMNN INR backbone; STRIDE-SIREN uses a SIREN backbone.

MODEL	DATASET →	<i>KS</i>	<i>FlowAO</i>	<i>SWE (128×128)</i>	<i>Seismic</i>
SHRED	$T_{train}$ (s)	1178.20	3502.07	2969.87	14356.15
	$T_{test}$ (s)	0.15	0.64	0.45	0.35
SHRED-ROM	$T_{train}$ (s)	2642.42	1549.72	2454.69	1293.78
	$T_{test}$ (s)	0.14	0.10	0.12	0.25
STRIDE-SIREN	$T_{train}$ (s)	4993.41	4335.55	5140.88	64340.34
	$T_{test}$ (s)	3.30	16.06	14.19	6.90
STRIDE-FMMNN	$T_{train}$ (s)	2076.49	3895.35	7203.90	97803.72
	$T_{test}$ (s)	3.35	13.93	17.82	14.57

These costs are the price of resolution-invariant reconstruction and improved expressivity. When super-resolution is not needed, the decoder can be evaluated on a coarser grid to trade accuracy for speed; more generally, future work could focus on accelerating INR inference (e.g., distillation to a lightweight grid decoder, hierarchical/coarse-to-fine querying, or caching on regular grids). Moreover, it remains to evaluate the framework on large-scale practical problems, particularly those characterized by higher-frequency components.

## 5 Conclusion

We introduced STRIDE, a two-stage framework for reconstructing spatiotemporal fields from sparse point-sensor measurements. STRIDE first maps a short observation window to a low-dimensional latent state using a temporal encoder, and then decodes the latent state with a coordinate-based implicit neural representation (INR) to produce continuous, resolution-invariant reconstructions. Across four benchmarks spanning chaotic dynamics and wave propagation, our default instantiation STRIDE-FMMNN achieves lower reconstruction errors than strong baselines and is more stable to train than the SIREN-backbone variant STRIDE-SIREN, while retaining the ability to super-resolve by querying the decoder at arbitrary spatial coordinates.

From a theoretical standpoint, we provided a justification for why a finite-dimensional latent state can suffice: under delay observability of point measurements on the relevant invariant set, the reconstruction operator factors through a finite-dimensional embedding, making STRIDE-type architectures natural approximators. A key limitation is the computational cost inherited from INR decoders, since reconstructing a full field requires many coordinate queries. Future work will focus on accelerating INR inference and scaling STRIDE to larger, higher-frequency problems and more challenging sensing regimes.

## Acknowledgment:

The authors thank Prof. Nathan Kutz for the motivating discussion during his visit to Georgia Tech, and Sebastian Gutierrez Hernandez for his group presentation on the FMMNN architecture [17]. This research was supported by NSF grant # 2325631.

## References

- [1] Steven Brunton, Bernd Noack, and Petros Koumoutsakos. Machine Learning for Fluid Mechanics. *Annual Review of Fluid Mechanics*, 52(1):477–508, January 2020. arXiv:1905.11075 [physics].
- [2] Rui Wang and Rose Yu. Physics-Guided Deep Learning for Dynamical Systems: A Survey, February 2023. arXiv:2107.01272 [cs].
- [3] N. Benjamin Erichson, Lionel Mathelin, Zhewei Yao, Steven L. Brunton, Michael W. Mahoney, and J. Nathan Kutz. Shallow Neural Networks for Fluid Flow Reconstruction with Limited Sensors. *Proceedings of the Royal Society A: Mathematical, Physical and Engineering Sciences*, 476(2238):20200097, June 2020. arXiv:1902.07358 [physics].
- [4] George Em Karniadakis, Ioannis G. Kevrekidis, Lu Lu, Paris Perdikaris, Sifan Wang, and Liu Yang. Physics-informed machine learning. *Nature Reviews Physics*, 3(6):422–440, June 2021. Publisher: Nature Publishing Group.
- [5] Javier E. Santos, Zachary R. Fox, Arvind Mohan, Daniel O’Malley, Hari Viswanathan, and Nicholas Lubbers. Development of the Senseiver for efficient field reconstruction from sparse observations. *Nature Machine Intelligence*, 5(11):1317–1325, November 2023. Publisher: Nature Publishing Group.
- [6] Xihaier Luo, Wei Xu, Yihui Ren, Shinjae Yoo, and Balu Nadiga. Continuous Field Reconstruction from Sparse Observations with Implicit Neural Networks, January 2024. arXiv:2401.11611 [cs].
- [7] Jan P. Williams, Olivia Zahn, and J. Nathan Kutz. Sensing with shallow recurrent decoder networks, June 2024. arXiv:2301.12011 [math].
- [8] Matteo Tomasetto, Jan P. Williams, Francesco Braghin, Andrea Manzoni, and J. Nathan Kutz. Reduced Order Modeling with Shallow Recurrent Decoder Networks, February 2025. arXiv:2502.10930 [cs].
- [9] Dongwei Lyu, Rie Nakata, Pu Ren, Michael W. Mahoney, Arben Pitarka, Nori Nakata, and N. Benjamin Erichson. WaveCastNet: An AI-enabled Wavefield Forecasting Framework for Earthquake Early Warning, May 2024. arXiv:2405.20516 [cs].
- [10] Jialin Song, Zeheng Song, Pu Ren, N Benjamin Erichson, Michael W Mahoney, and Xiaoye S Li. Forecasting high-dimensional spatio-temporal systems from sparse measurements. *Machine Learning: Science and Technology*, 5(4):045067, December 2024. Publisher: IOP Publishing.
- [11] Floris Takens. Detecting strange attractors in turbulence. In David A. Rand and Lai-Sang Young, editors, *Dynamical Systems and Turbulence, Warwick 1980*, volume 898 of *Lecture Notes in Mathematics*, pages 366–381. Springer, 1981.
- [12] Timothy Sauer, James A. Yorke, and Martin Casdagli. Embedology. *Journal of Statistical Physics*, 65(3-4):579–616, 1991.
- [13] Vincent Sitzmann, Julien N. P. Martel, Alexander W. Bergman, David B. Lindell, and Gordon Wetzstein. Implicit Neural Representations with Periodic Activation Functions, June 2020. arXiv:2006.09661 [cs].
- [14] Ethan Perez, Florian Strub, Harm de Vries, Vincent Dumoulin, and Aaron Courville. FiLM: Visual Reasoning with a General Conditioning Layer, December 2017. arXiv:1709.07871 [cs].
- [15] Louis Serrano, Lise Le Boudec, Armand Kassaï Koupaï, Thomas X. Wang, Yuan Yin, Jean-Noël Vittaut, and Patrick Gallinari. Operator Learning with Neural Fields: Tackling PDEs on General Geometries, November 2023. arXiv:2306.07266 [cs].
- [16] Pan Du, Meet Hemant Parikh, Xiantao Fan, Xin-Yang Liu, and Jian-Xun Wang. CoNFiLD: Conditional Neural Field Latent Diffusion Model Generating Spatiotemporal Turbulence, March 2024. arXiv:2403.05940 [physics].
- [17] Shijun Zhang, Hongkai Zhao, Yimin Zhong, and Haomin Zhou. Fourier Multi-Component and Multi-Layer Neural Networks: Unlocking High-Frequency Potential, June 2025. arXiv:2502.18959 [cs].
- [18] Sepp Hochreiter and Jürgen Schmidhuber. Long Short-Term Memory. *Neural Computation*, 9(8):1735–1780, November 1997.
- [19] Albert Gu and Tri Dao. Mamba: Linear-Time Sequence Modeling with Selective State Spaces, May 2024. arXiv:2312.00752 [cs].
- [20] Ricardo Mañé. On the dimension of the compact invariant sets of certain nonlinear maps. In *Dynamical Systems and Turbulence, Warwick 1980*, volume 898 of *Lecture Notes in Mathematics*, pages 230–242. Springer, 1981.
- [21] Junyoung Chung, Caglar Gulcehre, KyungHyun Cho, and Yoshua Bengio. Empirical Evaluation of Gated Recurrent Neural Networks on Sequence Modeling, December 2014. arXiv:1412.3555 [cs].

- [22] Yuan Qiu, Nolan Bridges, and Peng Chen. Derivative-enhanced Deep Operator Network, October 2024. arXiv:2402.19242 [cs].
- [23] Nikhil Vyas, Depen Morwani, Rosie Zhao, Mujin Kwun, Itai Shapira, David Brandfonbrener, Lucas Janson, and Sham Kakade. SOAP: Improving and Stabilizing Shampoo using Adam, January 2025. arXiv:2409.11321 [cs].
- [24] Francesco Regazzoni, Stefano Pagani, Matteo Salvador, Luca Dede', and Alfio Quarteroni. Learning the intrinsic dynamics of spatio-temporal processes through Latent Dynamics Networks. *Nature Communications*, 15(1):1834, February 2024. Publisher: Nature Publishing Group.
- [25] Roger Temam. *Infinite-Dimensional Dynamical Systems in Mechanics and Physics*, volume 68 of *Applied Mathematical Sciences*. Springer, 2 edition, 1997.
- [26] Phillip Si and Peng Chen. Latent-EnSF: A Latent Ensemble Score Filter for High-Dimensional Data Assimilation with Sparse Observation Data, September 2024. arXiv:2409.00127 [cs].
- [27] Fabio Luporini, Mathias Louboutin, Michael Lange, Navjot Kukreja, Philipp Witte, Jan Hückelheim, Charles Yount, Paul H. J. Kelly, Felix J. Herrmann, and Gerard J. Gorman. Architecture and performance of devito, a system for automated stencil computation. *ACM Trans. Math. Softw.*, 46(1), apr 2020.
- [28] Chengyuan Deng, Shihang Feng, Hanchen Wang, Xitong Zhang, Peng Jin, Yinan Feng, Qili Zeng, Yinpeng Chen, and Youzuo Lin. OpenFWI: Large-Scale Multi-Structural Benchmark Datasets for Seismic Full Waveform Inversion, June 2023. arXiv:2111.02926 [cs].
- [29] Niharika Karnik, Yash Bhangale, Mohammad G. Abdo, Andrei A. Klishin, Joshua J. Cogliati, Bingni W. Brunton, J. Nathan Kutz, Steven L. Brunton, and Krithika Manohar. PySensors 2.0: A Python Package for Sparse Sensor Placement, September 2025. arXiv:2509.08017 [cs].
- [30] Ken-Ichi Funahashi and Yuichi Nakamura. Approximation of dynamical systems by continuous time recurrent neural networks. *Neural Networks*, 6(6):801–806, 1993.
- [31] Kurt Hornik, Maxwell Stinchcombe, and Halbert White. Multilayer feedforward networks are universal approximators. *Neural Networks*, 2(5):359–366, 1989.
- [32] Moshe Leshno, Vladimir Y. Lin, Allan Pinkus, and Shimon Schocken. Multilayer feedforward networks with a nonpolynomial activation function can approximate any function. *Neural Networks*, 6(6):861–867, 1993.
- [33] Lisha Li, Kevin Jamieson, Giulia DeSalvo, Afshin Rostamizadeh, and Ameet Talwalkar. Hyperband: A Novel Bandit-Based Approach to Hyperparameter Optimization, June 2018. arXiv:1603.06560 [cs].

## A Proof

### A.1 Proof of Lemma 3.3

*Proof.* Let  $\iota : X \hookrightarrow C^0(\Omega, \mathbb{R}^{d_x})$  denote the continuous embedding, and define  $G_k : \mathcal{A} \rightarrow X$  by  $G_k(\mu, x) := F_\mu^k x$ . Then  $T(\mathbf{y}) = \iota(G_k(\Psi(\mathbf{y})))$ . Under Assumption 3.2,  $\Psi : Y \rightarrow \mathcal{A}$  is Lipschitz and hence continuous. By assumption,  $G_k$  is continuous on  $\mathcal{A}$ . Therefore, the composition  $\mathbf{y} \mapsto \iota(G_k(\Psi(\mathbf{y})))$  is continuous as a map from  $Y$  into  $C^0(\Omega, \mathbb{R}^{d_x})$ , which proves the continuity of  $T$ . For the stability bound, for any  $\mathbf{y}, \mathbf{y}' \in Y$  we have

$$\|T(\mathbf{y}) - T(\mathbf{y}')\|_{C^0} \leq C_{\text{ev}} \|G_k(\Psi(\mathbf{y})) - G_k(\Psi(\mathbf{y}'))\|_X,$$

where we used the embedding inequality. Using that  $G_k$  is  $L_{F^k}$ -Lipschitz on  $\mathcal{A}$  and  $\Psi$  is  $L_\Psi$ -Lipschitz on  $Y$ ,

$$\|G_k(\Psi(\mathbf{y})) - G_k(\Psi(\mathbf{y}'))\|_X \leq L_{F^k} \|\Psi(\mathbf{y}) - \Psi(\mathbf{y}')\|_{\mathcal{P} \times X} \leq L_{F^k} L_\Psi \|\mathbf{y} - \mathbf{y}'\|.$$

Combining the two displays yields the claimed inequality.  $\square$

### A.2 Proof of Theorem 3.4

*Proof.* Let  $q = (k+1)p$  and recall that  $Y = \Phi_k(\mathcal{A}) \subset \mathbb{R}^q$  is compact. Define the end-of-window state map  $U : Y \rightarrow X$  by

$$U(\mathbf{y}) := G_k(\Psi(\mathbf{y})) \in X, \quad \mathbf{y} \in Y.$$

Since  $\Psi$  is continuous on  $Y$  (Assumption 3.2) and  $G_k$  is continuous on  $\mathcal{A}$  by assumption,  $U$  is continuous. Moreover,  $U(Y) \subset \mathcal{A}_X$ .

Because  $\mathcal{A}_X$  is compact with finite box-counting dimension  $d_X$ , the Mañé projection theorem implies that for any integer  $d_z > 2d_X$  there exists a bounded linear map  $E : X \rightarrow \mathbb{R}^{d_z}$  that is injective on  $\mathcal{A}_X$  and admits a (Hölder, hence continuous) inverse  $E^{-1} : Z \rightarrow \mathcal{A}_X$  on  $Z := E(\mathcal{A}_X) \subset \mathbb{R}^{d_z}$  [20]. Define the latent map  $H : Y \rightarrow Z$  by  $H(\mathbf{y}) := E(U(\mathbf{y}))$ , which is continuous as a composition. Next define the decoder target  $D : \Omega \times Z \rightarrow \mathbb{R}^{d_x}$  by

$$D(\xi, z) := (E^{-1}(z))(\xi).$$

This is well-defined because  $E^{-1}(z) \in \mathcal{A}_X \subset X$  and point evaluation is continuous on  $X$ . Since  $E^{-1}$  is continuous on  $Z$  and  $(\xi, x) \mapsto x(\xi)$  is continuous on  $\Omega \times X$ ,  $D$  is continuous on the compact set  $\Omega \times Z$ . Finally, for any  $\mathbf{y} \in Y$  and  $\xi \in \Omega$ ,

$$T(\mathbf{y})(\xi) = U(\mathbf{y})(\xi) = (E^{-1}(H(\mathbf{y})))(\xi) = D(\xi, H(\mathbf{y})),$$

which proves the factorization.

For approximation, note that  $H$  is continuous on compact  $Y$  and  $D$  is continuous on compact  $\Omega \times Z$ . Hence  $D$  is uniformly continuous; let  $\omega_D$  be a modulus of continuity in its second argument:

$$\omega_D(r) := \sup \{ \|D(\xi, z) - D(\xi, z')\| : \xi \in \Omega, z, z' \in Z, \|z - z'\| \leq r \},$$

so  $\omega_D(r) \rightarrow 0$  as  $r \rightarrow 0$ . Fix  $\varepsilon > 0$  and choose  $\delta > 0$  such that  $\omega_D(\delta) \leq \varepsilon/2$ . By universal approximation on compact sets, there exist neural-network parametrizations  $\mathcal{G} : Y \rightarrow \mathbb{R}^{d_z}$  and  $\mathcal{F} : \Omega \times \mathbb{R}^{d_z} \rightarrow \mathbb{R}^{d_x}$  such that

$$\sup_{\mathbf{y} \in Y} \|H(\mathbf{y}) - \mathcal{G}(\mathbf{y})\| \leq \delta \quad \text{and} \quad \sup_{\xi \in \Omega, z \in Z} \|D(\xi, z) - \mathcal{F}(\xi, z)\| \leq \varepsilon/2,$$

for example using recurrent/window encoders for  $\mathcal{G}$  and feedforward/modulated networks for  $\mathcal{F}$  [30, 31, 32]. Then, for any  $\mathbf{y} \in Y$  and  $\xi \in \Omega$ ,

$$\begin{aligned} \|T(\mathbf{y})(\xi) - \mathcal{F}(\xi, \mathcal{G}(\mathbf{y}))\| &= \|D(\xi, H(\mathbf{y})) - \mathcal{F}(\xi, \mathcal{G}(\mathbf{y}))\| \\ &\leq \|D(\xi, H(\mathbf{y})) - D(\xi, \mathcal{G}(\mathbf{y}))\| + \|D(\xi, \mathcal{G}(\mathbf{y})) - \mathcal{F}(\xi, \mathcal{G}(\mathbf{y}))\| \\ &\leq \omega_D(\|H(\mathbf{y}) - \mathcal{G}(\mathbf{y})\|) + \varepsilon/2 \leq \omega_D(\delta) + \varepsilon/2 \leq \varepsilon, \end{aligned}$$

which concludes the proof.  $\square$

*Remark A.1* (Approximate embedding and an error floor). Assumption 3.2 is an idealization: with finite sampling, sensor noise, and limited sensor budgets, the delay map  $\Phi_k$  may fail to be exactly injective on  $\mathcal{A}$ , or it may be injective but poorly conditioned. Two standard relaxations make the stability picture explicit. (i) *Injective but not Lipschitz*. If  $\Phi_k$  is injective on  $\mathcal{A}$  but the inverse is only uniformly continuous, one may replace the Lipschitz bound in Assumption 3.2 by a modulus of continuity  $\omega$  such that

$$\|\Psi(\mathbf{y}) - \Psi(\mathbf{y}')\|_{\mathcal{P} \times X} \leq \omega(\|\mathbf{y} - \mathbf{y}'\|), \quad \mathbf{y}, \mathbf{y}' \in Y. \quad (19)$$

Then the stability estimate becomes

$$\|T(\mathbf{y}) - T(\mathbf{y}')\|_{C^0} \leq C_{\text{ev}} L_{F^k} \omega(\|\mathbf{y} - \mathbf{y}'\|), \quad (20)$$

so observation perturbations translate into reconstruction perturbations according to the (possibly sub-Lipschitz) conditioning encoded by  $\omega$ . (ii) *Non-injective (intrinsic ambiguity)*. If  $\Phi_k$  is not injective, a useful identifiability proxy is the ambiguity function

$$\alpha(\varepsilon) := \sup \left\{ \|G_k(a) - G_k(a')\|_X : a, a' \in \mathcal{A}, \|\Phi_k(a) - \Phi_k(a')\| \leq \varepsilon \right\}, \quad (21)$$

where  $a = (\boldsymbol{\mu}, \mathbf{x})$  denotes the augmented state and  $G_k(\boldsymbol{\mu}, \mathbf{x}) := F_{\boldsymbol{\mu}}^k \mathbf{x}$  is the end-of-window state. When  $\alpha(\varepsilon) > 0$ , two distinct augmented states (potentially with different  $\boldsymbol{\mu}$ ) can generate  $\varepsilon$ -close observation windows, so no method that uses only the window can guarantee reconstruction error below order  $C_{\text{ev}} \alpha(\varepsilon)$  (with  $\varepsilon$  set by noise/discretization). Both viewpoints motivate increasing the window length (larger  $k$ ) and/or the number of sensors (larger  $p$ ) until the empirical mapping becomes sufficiently well-conditioned, as explored in our ablation studies.

## B Training Details

To determine the optimal hyperparameter choices for STRIDE-FMMNN in all the examples, we conduct the hyperparameter search using Bayesian optimization [33]. The range of hyperparameters considered is listed in Table 6. The details of STRIDE training (including STRIDE-FMMNN and STRIDE-SIREN) and optimized hyperparameters are shown in Table 7. SHRED and SHRED-ROM have the same temporal decoder as STRIDE, and have a shallow decoder with 2 hidden layers of 350 and 400 neurons, respectively, which is the same as the default setting in [8]. For all the trained models, we employ an early stopping mechanism: the training terminates once the validation loss does not decrease by more than 0.5% in 10 epochs over an 80-epoch period.

Table 6: Hyperparameter search range for STRIDE-FMMNN training

HYPERPARAMETER	<i>KS</i>	<i>FlowAO</i>	<i>SWE (128×128)</i>	<i>Seismic</i>
NUMBER OF LATENT STATES	16 – 128	16 – 128	32 – 256	32 – 256
DECODER DEPTH	2 – 10	2 – 10	3 – 12	3 – 12
DECODER RANK	16 – 128	16 – 128	32 – 256	32 – 256
DECODER WIDTH	256 – 2048	256 – 2048	256 – 2048	256 – 2048
FOURIER EMBEDDING DIM	0 – 50	0 – 50	0 – 50	0 – 50
LEARNING RATE	1E-3 – 5E-3	1E-3 – 5E-3	1E-3 – 5E-3	1E-3 – 4E-3
BATCH SIZE	128 – 1024	16 – 128	16 – 128	64 – 128

Table 7: Training details for STRIDE

HYPERPARAMETER	<i>KS</i>	<i>FlowAO</i>	<i>SWE (128×128)</i>	<i>Seismic</i>
LAG	50	50	50	50
NUMBER OF SENSORS	2	3	100	100
NUMBER OF SPACE POINTS	100	5000	4096	4900
NUMBER OF LATENT STATES	128	64	128	256
NUMBER OF HIDDEN LAYERS	2	2	2	2
FMMNN DECODER DEPTH	3	6	8	4
FMMNN DECODER RANK	128	32	32	128
FMMNN DECODER WIDTH	1024	256	256	1024
SIREN DECODER DEPTH	3	6	8	4
SIREN DECODER WIDTH	384	96	96	384
FOURIER EMBEDDING DIM	0	5	20	5
FMMNN LEARNING RATE	3E-3	3E-3	2E-3	3E-3
SIREN LEARNING RATE	1E-4	1E-4	1E-4	1E-4
SCHEDULER GAMMA/PATIENCE	0.4/10	0.4/10	0.4/10	0.4/10
BATCH SIZE	256	128	128	128

Tables 8 and 9 specify the training details for the auxiliary models used in parameter estimation (see Fig. 15) and forecasting (see Fig. 16).

Table 8: Training details for auxiliary MLP (parameter estimation)

HYPERPARAMETER	<i>SWE (128×128)</i>	<i>FlowAO</i>
LATENT DIMENSION	128	64
HIDDEN DIMENSION	128	64
NUMBER OF HIDDEN LAYERS	2	2
PARAMETER DIMENSION	2	1
ACTIVATION FUNCTION	GELU	GELU
LEARNING RATE	2E-4	5E-4
NUMBER OF EPOCHS	2000	2000
BATCH SIZE	1024	1024

Table 9: Training details for auxiliary LSTM (forecasting)

HYPERPARAMETER	<i>SWE (128×128)</i>	<i>Seismic</i>
INPUT LENGTH	20	20
OUTPUT LENGTH	1	1
LATENT DIMENSION	128	256
HIDDEN DIMENSION	256	256
NUMBER OF HIDDEN LAYERS	2	2
LEARNING RATE	1E-3	1E-3
SCHEDULER GAMMA/PATIENCE	0.5/10	0.5/10
NUMBER OF EPOCHS	400	400
DROPOUT	0.1	0.1
BATCH SIZE	1024	1024